ACS OMEGA

Open Access

http://pubs.acs.org/journal/acsodf

Article

Optical Monitoring of Labile Zinc inside Metastatic Cells with Plasmonic Chemonanosensors

Published as part of ACS Omega virtual special issue "Celebrating 50 Years of Surface Enhanced Spectroscopy".

Ting Zhou, Rubén Vicente, and Pilar Rivera-Gil*

Cite This: *ACS Omega* 2024, 9, 42183−42192

Read Online

ACCESS | Metrics & More | Article Recommendations | Supporting Information

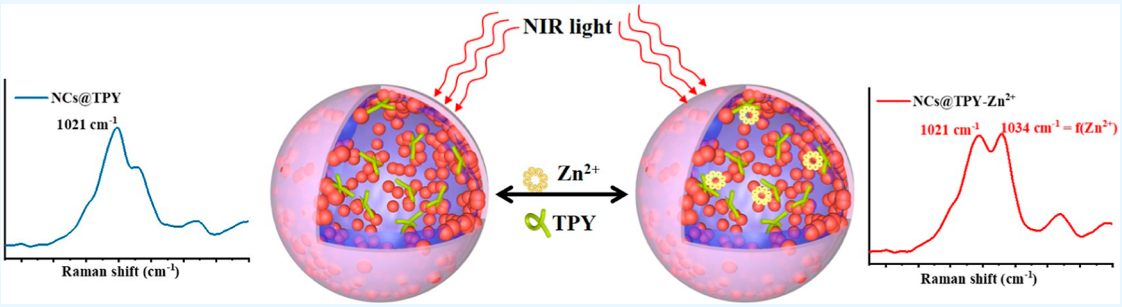

ABSTRACT: We report the development and characterization of an optical nanosensor for the detection of labile zinc in biological environments. The readout is based on surface-enhanced Raman scattering promoted by a Raman reporter conjugated to the inner plasmonic cavity of hollow silica nanocapsules. We quantify Zn^{2+} by obtaining the ratio between a Zn^{2+}-sensitive band and a Zn^{2+}-insensitive band. The Raman reporter measures within the range from 10^{-5} to 10^{-11} M and exhibits a limit of detection of $10^{-11.72}$ M. The nanosensor discriminates between intracellular and extracellular Zn^{2+} concentrations.

INTRODUCTION

Zinc and its structural role are ubiquitous and are of outstanding importance for human health. It is a highly versatile metal with a flexible metal's coordination geometry, participating in ligand binding, catalytic enzymes' activity, biological membranes, gene expression, and endocrine system.[1] Because of zinc's ubiquity and versatility, imbalances of its homeostasis result in a generalized damage of human health and are responsible for many diseases.[2] Zinc dyshomeostasis is involved in Alzheimer[3] and, more generally, in neuronal injury in brain diseases. Brain is the organ containing the highest amount of zinc (mM).[4] For example, it is known that during stroke, seizures, or mechanical head injuries, there is an increased level of zinc released to the synaptic space, causing neuronal injury or death.[5] Clinical studies have shown that low serum zinc levels are associated with high brain amyloid deposition responsible for Alzheimer's disease.[6] Zinc is referred to as an insulin mimetic because it activates lipogenesis and the insulin-signaling cascade.[7] A prospective cohort study in women from USA demonstrated that low zinc intake increases 17% the risk of developing diabetes. Inadequate zinc distribution affects diabetes,[7] sarcopenia, and adipocyte metabolism- and other metabolism-associated disorders.[2] Zinc imbalances are also involved in cancer with special relevance in metastasis. High serum copper/zinc ratios are found in patients with lung, breast, gastrointestinal tract, and gynecological tumors. Low levels of zinc increase the proliferation of esophageal cells and the risk of developing esophageal squamous cell carcinoma. A marked decrease in zinc levels has been found in leukemic leukocytes and in malignant prostate cancer cells, being the last and the most consistent and persistent biochemical feature of prostate malignancies.[8]

These observations demonstrate that zinc is a candidate biomarker or a therapeutic target for many pathological conditions.[9] Therefore, it is crucial to find methodologies to quantify zinc dynamics in cells, fluids, and tissues.

Zinc is mostly found tightly bound to proteins; however, there is an equilibrium with mobile zinc pools. Labile zinc (Zn^{2+}) can be found in organs like the brain, retina, pancreas, and prostate.[1] When interrogating mobile zinc, it is crucial that the sensor rapidly and selectively binds Zn^{2+} to prevent it from reaching its natural target. Otherwise, it can lead to false conclusions about zinc function.[10] Zn^{2+} ranges from mM within the synaptic vesicles at glutamatergic nerve terminals to

Received: April 15, 2024
Revised: July 15, 2024
Accepted: July 17, 2024
Published: October 3, 2024

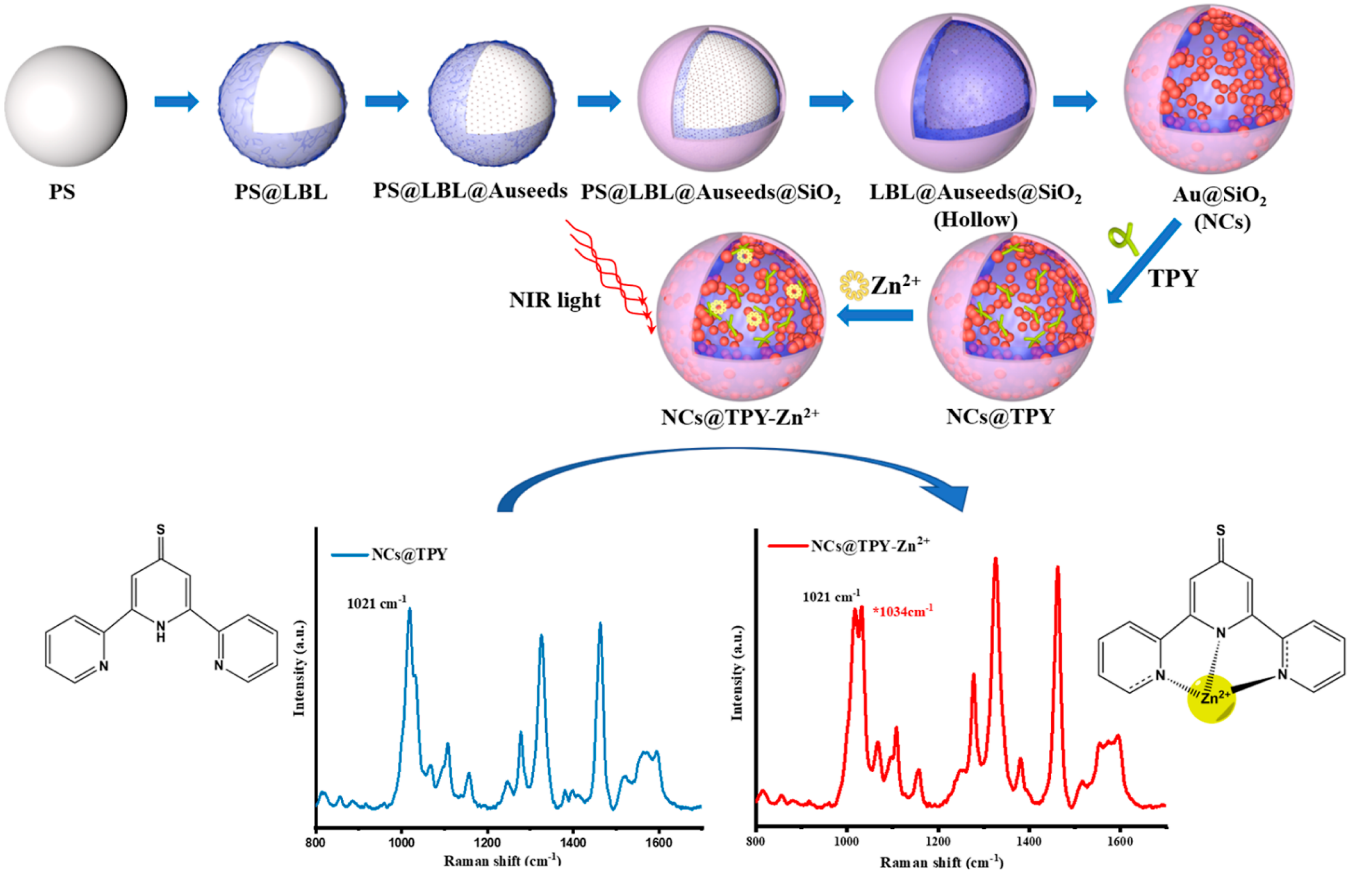

Figure 1. Schematic representation of the working principle of our Raman probe for Zn^{2+}.

nM within the cell cytosol.[4] Therefore, it is also key that the sensor responds to a wide range of Zn^{2+} amounts.

Because of its electronic configuration, Zn^{2+} does not provide a spectroscopy or magnetic signal as other transition metal ions do. Zn^{2+} ions are spectroscopically silent (d^{10} systems),[1] and regular analytical techniques cannot be used. Zn^{2+} can be histochemically detected; however, it is not compatible with dynamic or live experiments.[10] Zn^{2+} can be chelated with an appropriate luminescent probe; thus, fluorescence remains the gold standard. Fluorescent zinc probes respond rapidly, are specific, and have spatial (subcellular) and temporal resolution. Nevertheless, fluorescence techniques have intrinsic drawbacks such as a lack of photostability (photobleaching), solubility, selectivity (cross-talk mostly with Ca^{2+} and Mg^{2+}), and sensitivity (μM) and limited multiplexing.

By comparison, surface-enhanced Raman spectroscopy (SERS) is a highly sensitive and specific multiplexing tool to probe analytes.[11,12] SERS tracks chemical modifications of a Raman probe (with a high Raman cross-section) that is attached onto a plasmonic nanostructure since analyte recognition induces characteristic and unique spectral changes.[13,14] SERS measures the molecular fingerprint of the probe. Most of the SERS sensors carry the probe outside at the interface with the environment. This has an impact on the sensitivity and reliability of the sensor's quantification because the probe can be replaced by specific biomolecules (e.g., glutathione) and/or the close contact of biomolecules to the plasmonic surface interferes with the Raman probe signal.

In this study, we have widened our tool of SERS nanoprobes[13,15,16] by designing a Zn^{2+} nanosensor. Our nanosensor locates the Raman probe in the cavity of a porous capsule that allows the diffusion of ions but not of biomolecules; it exhibits interparticle hot spots concentrated in the inner shell, it provides ratiometric measurements, and it is noninvasive and can quantify the analyte in real time and with spatiotemporal resolution. All of this ensures that the signal of our nanosensor is stable and reproducible. This tool of nanosensors aims at quantifying analyte dynamics inside living cells. Specifically, for Zn^{2+}, we focus on correlating how Zn^{2+} dynamics occur in metastatic cells vs their parental (nonmetastatic) cells.

MATERIALS AND METHODS

Materials. 2,2′:6′,2″-Terpyridine-4′-thiol (TPY) was purchased from ALFA Chemistry. Polyvinylpyrrolidone (PVP, MW: 10,000), 2,2′-azobis (2-methylpropionamidine) dihydrochloride (AIBA), styrene, polysodium(styrenesulfonate) (PSS, MW: 70,000), poly(allylamine hydrochloride) (PAH, MW: 50,000), tetrakis (hydroxymethyl) phosphonium chloride solution (THPC), Gold(III) chloride trihydrate, ammonia solution, tetraethyl orthosilicate (TEOS), phosphoric acid, sodium phosphate monobasic, sodium phosphate dibasic, zinc sulfate heptahydrate ($ZnSO_4{\cdot}7H_2O$), calcium chloride ($CaCl_2$), and Zinquin were purchased from Sigma-Aldrich. Sodium hydroxide, puromycin, and the cell counting chamber slide were purchased from Thermo Fisher. Chloroform was purchased from Scharlau. The ibidi glass bottom dish (35 mm)

https://doi.org/10.1021/acsomega.4c03631
ACS Omega 2024, 9, 42183−42192

was purchased from ibidi GmbH. All of the chemicals were used without further purification.

Synthesis of Au@SiO_2 Nanocapsules. Nanocapsules (NCs) were synthesized by the method reported earlier.[17] The methodology is based on layer-by-layer (LBL) assembly of polyelectrolytes of opposite charge wrapped around a sacrificial colloidal template, which is further functionalized according to the requirements.

The entire synthesis process of NCs can be roughly divided into 6 steps (Figure 1). Polystyrene (PS) beads with a diameter of 400 ± 50 nm served as templates and were synthesized as previously reported.[17] Polymerization was carried out with AIBA as an initiator. Styrene was added to the PVP and AIBA mixture at 70 °C. The reaction was kept at 70 °C for 24 h. The PS beads were diluted in ethanol up to 14 mg/mL under sonication for approximately 30 min to obtain monodisperse PS templates. For the LbL procedure on the PS templates, we prepared a water solution of the negatively and positively charged polyelectrolyte, PSS, and PAH (1 mg/mL in 0.5 M NaCl). PS solution was added dropwise to the PSS solution (3 times volume of PS) under sonication for approximately 30 min, followed by 1 h incubation at room temperature to allow the electrostatic adsorption of PSS to the PS templates. The excess PSS was removed by three centrifugation cycles (8500 rpm, 25 min). These steps of polyelectrolyte adsorption and rinsing were repeated consecutively for PAH, PSS, and PAH. At the end, we obtain the PS templates with four monolayers of alternating polyelectrolytes (PS@LbL). The next step is to functionalize the LbL with a gold nanostructure for Raman enhancement. To this end, we synthesized gold seeds (3−5 nm, negatively charged) and then added them to PS@LbL as an extra layer of the LbL assembly (PS@LbL@Auseeds). The PS@LbL@Auseeds structures were coated with a PVP layer and combined with TEOS to form a silica layer (approximately thickness 20 nm) (PS@ LbL@ Auseeds@SiO_2). The PS templates were dissolved with an ethanol/chloroform (v/v = 1:3) mixture, and hollow NCs were obtained (LBL@Auseeds@SiO_2 (hollow). To enhance the Raman signal, Au seeds were grown in situ to build an inner plasmonic nanostructure through catalyzed reduction of Au ions with formaldehyde (NCs). NaOH solution (0.2 M, 6 mL) and THPC solution (1.2%, 4 mL) were added to 182 mL of water and mixed under stirring for 2 min. Finally, $HAuCl_4$ (25 mM, 8 mL) was added to the mixture quickly in one pot. The solution's color turns deep brown immediately. The dispersion was stirred continuously for around 10 min. After each step, we wash 3 times to remove unbound material. We estimated the concentration of NCs by the initial PS weight. To this end, we dehydrate 1 mL of PS solution in an oven (40 °C) for approximately 6 h, and then, we weigh it. We assumed no loss during the synthesis process; therefore, the amount of PS corresponds to the amount of NCs.

Synthesis of the Zn^{2+}-Nanosensor and Stability of Its Signal to pH. TPY is selected as the sensing molecule of Zn^{2+} because it can tightly chelate Zn^{2+} through the nitrogen atoms of the TPY moiety.[18,19] Thanks to the presence of thiol groups, TPY can bind to the gold nanostructure of the NCs. To ensure a sufficient readout signal, we defined which TPY concentration (i) and conjugation reaction time (ii) are most convenient. (i) Equal volumes of different TPY concentrations (5, 50, and 500 μM) were added to the NCs under stirring for 24 h. We rinsed the NCs by centrifugation (4500 rpm, 10 min) 4 times and resuspended them into ethanol. (ii) We added 500 μM TPY to the NCs and allowed the reaction to take time over 0.5, 1, 3, 6, 12, and 24 h, followed by washing as described before. Both (i and ii) sets of samples were characterized with the Raman spectrophotometer, and the condition providing the best SERS signal was selected. We chose 500 μM TPY for 24 h to synthesize the nanosensors (NCs@TPY).

To study the stability of the SERS signal to pH, we prepared 100 mM phosphate buffer with pH ranging from 3 to 9 using phosphoric acid, sodium phosphate monobasic, and sodium phosphate dibasic. We added 500 μL of 0.5 mg/mL NCs@ TPY to 500 μL of 500 μM TPY under different pH environments (pH 3, 4, 5, 6, 7, 8, and 9) for 3 h.

Physicochemical Characterization. NCs@TPY stored at 4 °C was characterized by spectrophotometry (UV−visible and Raman), dynamic light scattering (DLS), and transmission electron microscopy (TEM) immediately after the synthesis and 6 months later to ensure signal stability.

Transmission Electron Microscopy. We used a JEOL JEM 1010 TEM instrument operating at an acceleration voltage of 80 kV with a tungsten filament. The samples were dispersed into ethanol solution. The samples were dropped onto Formvar/carbon-supported copper grids (200 mesh, TED PELLA INC., USA) and left to dry at room temperature overnight.

UV−Visible Spectroscopy. The absorption spectrum of each synthetic intermediate was measured with an UV−vis spectrometer (GE Healthcare Ultrospec 2100 pro), using a 600 μL black quartz cuvette. With water as the reference, we scanned the sample after reference adjustment. Wavelength scan was performed from 200 to 900 nm, with an interval of 1 nm.

Dynamic Light Scattering. The hydrodynamic diameter and zeta potential were measured with a Zetasizer Nano ZS (Malvern Instruments, UK). Each sample was diluted to 0.02 mg/mL in water. A folded capillary cell (Malvern Instruments, UK) was used for zeta potential measurement, and disposable "PS" cuvettes (Sigma-Aldrich, Darmstadt, Germany) were used for hydrodynamic diameter measurement, with the refractive index at 0.2 and absorption at 3.32. Every sample was measured 3 times, and each measurement took 10 runs.

Surface-Enhanced Raman Spectroscopy. We used a Renishaw's inVia Qontor Raman system equipped with a confocal optical microscope, 1200 l/mm grating, an NIR laser (785 nm), and a Peltier cooled CCD array detector. NCs@ TPY located in a glass bottom dish (ibidi) was placed under the microscope, and the laser was carefully focused onto NCs@TPY. We used a 60× (NA 1.00) water immersion objective to measure the NCs@TPY. This condition provides a laser spot diameter of approximately 1 μm, thus covering all the NCs@TPY area. Inelastic radiation was collected and analyzed using the windows-based Raman environment (Wire) software.

SERS Data Processing. The preprocessing steps were done with Spyder (anaconda3). The spectral baseline was subtracted by an asymmetric least-squares smoothing algorithm in order to eliminate the auto fluorescence background.[20] And we randomly selected 5 points for each sample to obtain the SERS spectrum and calculated the average spectrum for subsequent data processing.

Zn^{2+} Quantification in Solution and Calibration Curve. We dissolved $ZnSO_4$ into phosphate buffer or cation-depleted growth media [0.5% (v/v)] to obtain dispersion media with Zn^{2+} concentrations ranging from 10^{-5} to 10^{-12} M.

https://doi.org/10.1021/acsomega.4c03631
ACS Omega 2024, 9, 42183−42192

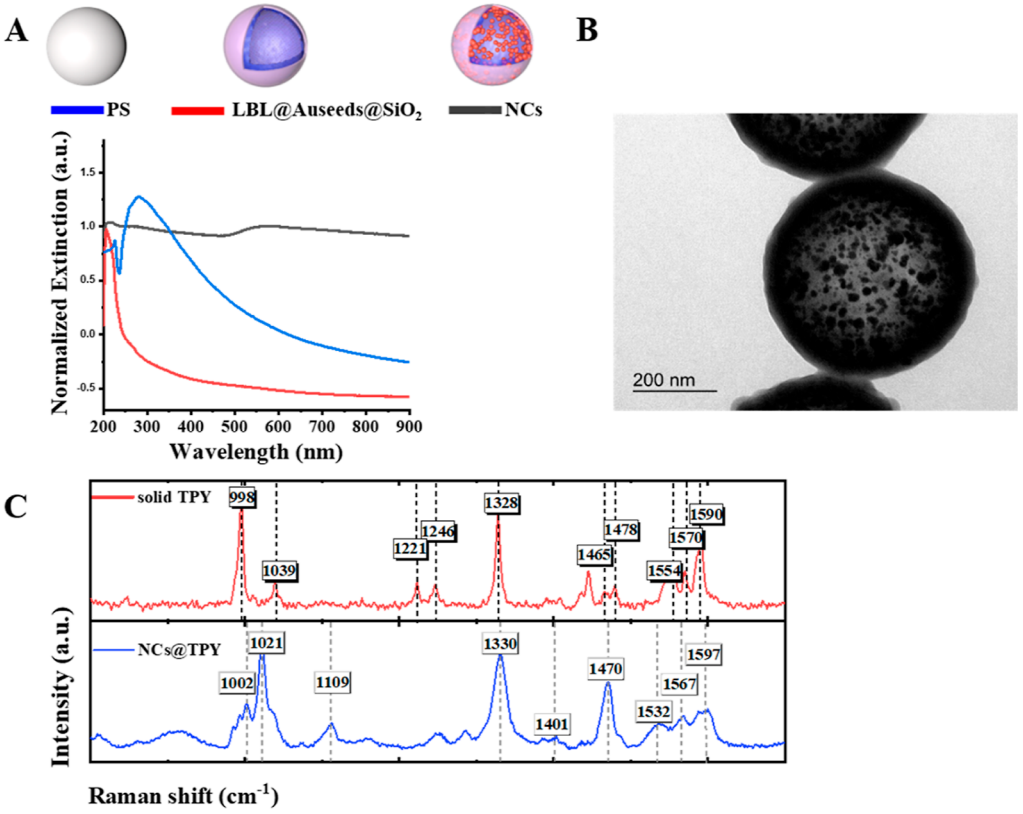

Figure 2. Synthesis and characterization of NCs@TPY. (A) UV−visible extinction profile of the NCs at different stages of the synthesis, i.e., PS template (blue), hollow with gold seeds (Auseeds@SiO_2; red), and NCs after growing the gold seeds (Au@SiO_2; black); (B) TEM image of Au@SiO_2 NCs; and (C) Raman spectrum (red) of TPY in the powder form and SERS spectrum (blue) of the TPY attached to the plasmonic nanostructure of the NCs (NCs@TPY).

NCs@TPY (0.25 mg/mL, calculated by the number of NCs) was dispersed into the corresponding media 30 min before SERS measurements. The integration time was set to 1 s, and the power at the sample was set to 0.35 mW.

For each concentration gradient sample (10^{-5} to 10^{-12} M), each spectrum was the average of 5 spectra. We used the average spectrum for division by nonsensitive peak intensity. The ratio of the sensitive peak intensity (I_{1034}) to the nonsensitive peak intensity (I_{1021}) is used as the *y*-axis, and the logarithmic of the Zn^{2+} concentration is used as the *x*-axis to establish a calibration curve by linear regression fitting.

Calcium Measurements with NCs@TPY. Similar to Zn^{2+} measurements, $CaCl_2$ was dissolved into cation-depleted growth media [0.5% (v/v)] to obtain a dispersion medium with a fixed concentration of Ca^{2+} ranging from 10^{-5} to 10^{-12} M. NCs@TPY (0.25 mg/mL as calculated by the number of NCs) was dispersed into the corresponding media 30 min before SERS measurements. The integration time was set to 1 s, and the power at the sample was set to 0.35 mW.

Each sample took 5 random measurements, and these 5 spectra were averaged. The ratio of the sensitive peak intensity (I_{1037}) to the nonsensitive peak intensity (I_{1026}) is used as the *y*-axis, and the logarithmic of the calcium concentration is used as the *x*-axis to establish a calibration curve by linear regression fitting.

Cell Culture. We used the brain metastatic breast cancer cell line MDA-MB-BrM2 (BrM2), lung metastatic breast cancer cell line MDA-MB-LM2 (LM2) (kindly provided by Joan Massagué from the Memorial Sloan Kettering Cancer Center, New York City, NY, USA), and parental cell line MDA-MB-231 (MDA), which is nonmetastatic. Thereby, we modified MDA-MB-231 to constitutively overexpress Zip4 (MDA-Zip4) and to study its role in Zn^{2+} imbalances. In short, the Zip4 cell line was generated by using a pMSCVpuro-hZip4 plasmid and selected with 0.25 μg/mL puromycin in the growth medium. The selection was removed to carry out the experiments.

Cells were cultured in Dulbecco's modified Eagle's medium/nutrient mixture F-12 (DMEM/F12, Thermo Fisher) supplemented with 10% fetal bovine serum (FBS), 1% L-glutamine, and 1% penicillin−streptomycin at 37 °C in a humidified 5% CO_2 atmosphere.

To fabricate a Zn^{2+}-free growth medium, we prepared the FBS with Chelex 100 resin (Bio-Rad Laboratories, Hercules, CA, USA) according to the manufacturer's instructions. These resins remove all divalent cations such as Zn^{2+}, Ca^{2+}, and Mg^{2+}. $ZnSO_4$ was then added as needed to the Zn^{2+}-free growth medium to obtain growth media at fixed Zn^{2+} concentrations.

Zn^{2+} Measurements with Zinquin. Five × 10^4 cells/mL of each cell line, MDA, MDA-Zip4, LM2, and BrM2, were seeded and grown onto glass bottom ibidi dishes until reaching 80−90% confluence. Cells were incubated with the growth media containing different concentrations (0, 10, 50, and 100 μM) of $ZnSO_4$ for 2 h. Afterward, cells were rinsed and were incubated with the Zn^{2+} dye, Zinquin (10 μL, 25 mM), for 30 min at 37 °C (5% CO_2) in 10 mL of isotonic solution. The isotonic solution contains (in millimoles) 140 NaCl, 5 KCl, 1.2 $CaCl_2$, 0.5 $MgCl_2$, 5 glucose, and 10 Hepes (300 mmol/liter, pH 7.4) plus different concentrations of Zn^{2+}. Cells were then detached with 0.05% trypsin in 0.53 mM EDTA and washed

https://doi.org/10.1021/acsomega.4c03631
ACS Omega 2024, 9, 42183−42192

with PBS. Fluorescence was quantified using an LSRII flow cytometer. Further analysis was performed using flow-through software (Turku Bioscience, Turku, Finland).

Cellular Mapping of Zn^{2+} with SERS. The same as with the Zn^{2+} measurements with Zinquin, 4 cell lines (5×10^4 cells/mL of each MDA, MDA-Zip4, LM2, and BrM2) were seeded and grown onto glass bottom dishes (ibidi) until reaching 80−90% confluence. Then, NCs@TPY (5 μg/mL) was incubated with four kinds of cells for 24 h in a cell growth medium without Zn^{2+}. After, the medium was removed and washed twice with PBS so that the NCs@TPY that is not inside the cells can be removed. Cells were incubated in media with different concentrations of Zn^{2+} (0, 10, 50, 100 μM) for 2 h.

SERS detection was performed via a 60× immersion objective and power ≤10%. Each sample was scanned at 3 arbitrary positions by Raman mapping. And the area of each position is 23 × 21 μm and consists of 56 spectra. The ratio of the sensitive peak intensity to nonsensitive peak intensity is used as the display intensity of scanning imaging. Brighter means a larger ratio.

Zn^{2+} Quantification with NCs@TPY in Metastatic vs Parental Cells. All four cell lines (5×10^4 cells/mL) were grown onto glass bottom dishes (diameter 35 mm). After reaching 80−90% cell confluency, we changed the growth medium into the cation-depleted growth medium. NCs@TPY (5 μg/mL) was added to the cells for 24 h. Cells were washed twice with PBS before adding the corresponding depleted medium (2 mL) containing a specific Zn^{2+} concentration (range: 10^{-5} to 10^{-12} M) for 2 h. In vitro SERS measurements were carried out at a laser power of 0.35 mW and an exposure time of 5 s.

For the intracellular Zn^{2+} measurements, we select individual NCs that are in the focal plane of the nucleus, thus being sure that they are inside. And for extracellular Zn^{2+}, we select individual nanoparticles dispersed in the culture medium.

For each concentration (10^{-5} to 10^{-12} M), we represent the average of five normalized intensity ratios. We set the insensitive peak intensity at 1021 cm^{-1} (I_{1021}) for each concentration to 1 and then calculated the intensity ratio, sensitive (1034 cm^{-1}) vs insensitive (I_{1034}/I_{1021}).

RESULTS AND DISCUSSION

Synthesis and Characterization of the Nanosensor (NCs@TPY). The NCs were synthesized by the method reported earlier.[13,15,17] The methodology is based on LBL assembly of polyelectrolytes of opposite charge wrapped around a sacrificial colloidal template, which is further functionalized (see the Materials and Methods section). Briefly, we synthesized plasmonic hollow NCs consisting of a silica shell and with a high intensity of plasmonic gold nanostructures in the innermost layer. The inner plasmonic nanostructure was further functionalized with the sensor molecule. The main reasons for this design are that (i) resonance couplings are generated in the inner plasmonic nanostructure under light irradiation, thereby forming a "hot spot", which greatly enhances the SERS signal of the Raman sensor molecule, and (ii) the silica shell protects the sensor molecule and reduce noise produced by the competitive adsorption of biological molecules to the plasmonic enhancing surface. This geometry allows our NCs to detect trace small analytes in complex biological samples.[21] Figure 1 shows a schematic representation of the complete procedure.

Figure 2 shows the NCs' main physicochemical characteristics. It can be seen from the UV−vis spectrum (Figure 2A) that when the template (blue line) is dissolved (red line), its corresponding extinction peak at approximately 280 nm disappears. A new extinction peak in the region 550−900 nm appeared after growing the gold seeds into nanostructures inside the NCs (gray line). There is no characteristic localized surface plasmon resonance of the good seeds (red line) because of their small size (3−5 nm). TEM (Figure 2B and cf. S1A) and DLS confirm the homogeneity of the NCs in suspension, showing an average hydrodynamic size of 455.1 ± 13.3 nm with PDI = 0.087 and a zeta potential value of −22.4 mV (cf., Figure S1B) due to the presence of deprotonated silanol groups in the silica shell. Figure 2C shows the Raman spectrum of TPY in the powder form (red line) and the SERS spectrum of TPY-modified NCs (NCs@TPY; blue line) in water. The difference in spectral fingerprints between the two spectra is the result of changes in the surface selection rules, as well as surface enhancement due to media interaction and resonant coupling occurring when TPY is adsorbed onto the metallic surface of NCs. It is worth noting that the characteristic SERS peaks of TPY appeared in the spectra of NCs@TPY, which confirmed the successful modification of TPY onto NCs.[22,23] Details of characteristic features (cf., Figure S1C) include the bands at 1002 cm^{-1} assigned to single pyridine ring breathing, at 1021 cm^{-1} resulting from terpyridine ring breathing, at 1330 cm^{-1} attributed to C−S ring breathing, at 1470 cm^{-1} issued from C−N stretching modes, and at 1532, 1567, and 1597 cm^{-1} referred to the C−C ring stretching mode.[24,25]

Subsequently, we changed different parameters like conjugation time and TPY concentration to select the most stable SERS signal (cf., Figure S2A,B). With the increase of the reaction time, the SERS characteristic peak intensity (I_{1021}) of TPY first increased and then decreased, and the signal intensity gradually stabilized after 24 h. The SERS intensity also increased with the increase of TPY concentration, 500 μM being the solubility limit. Therefore, the optimal conjugation conditions were established as 24 h reaction time and 500 μM TPY concentration.

One important issue to consider for SERS biosensors when interacting with living cells is signal stability,[21] specially against the different pH values existing inside cells. Most of the nanoparticles enter the cells through active internalization mechanisms, thus being incorporated in different phago-/endocytic vesicles exhibiting pH gradients from approximately 4 to 7.5.[26] We also know that pH alters the SERS readout because it affects the ionic strength of the environment surrounding the Raman sensor.[15,16,27] Specifically, for our sensor molecule TPY, it contains a terpyridine group. Pyridine groups are not in a fully protonated state even in acidic environments,[24] which means that the pH has little effect on the frequency of the ring-breathing mode. Furthermore, terpyridine ligands are rigid and form closed-shell octahedral TPY−metal^{2+}−TPY combinations. These complexes are robust even in challenging biological environments.[28]

Therefore, we studied the SERS signal stability of our NCs@TPY at different pH values. Our results confirmed that pH values between 3 and 9 have no effect on the SERS spectra of TPY (cf., Figure S2C). Following the study of signal stability, we tested it over time up to 6 months. We found no big changes in the geometry, absorption, or SERS profile (cf., Figure S2D,F). These results confirm SERS signal stability of

https://doi.org/10.1021/acsomega.4c03631
ACS Omega 2024, 9, 42183−42192

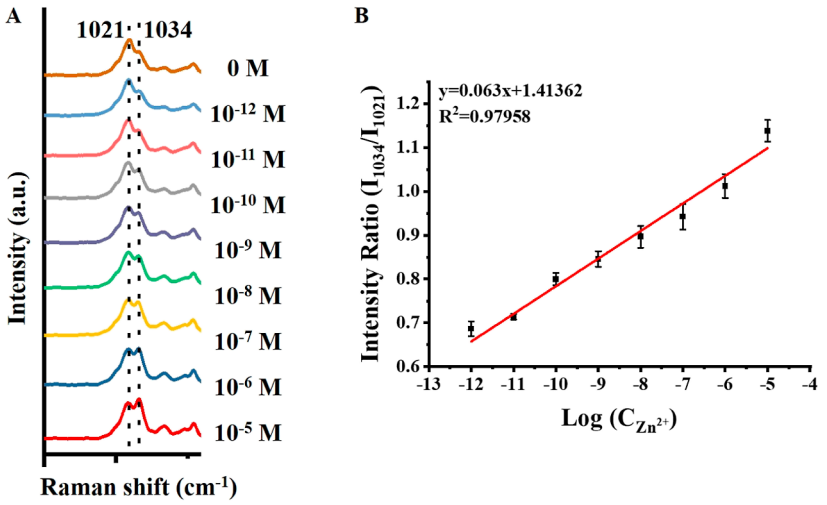

Figure 3. Calibration curve between the Zn^{2+}concentration in biological media and ratiometric SERS sensing. (A) SERS spectrum of NCs@TPY exposed to different Zn^{2+} concentrations (10^{-5}, 10^{-6}, 10^{-7}, 10^{-8}, 10^{-9}, 10^{-10}, 10^{-11}, and 10^{-12} M and none) in ion-depleted cell growth medium. The Zn^{2+}-sensitive (1034 cm^{-1}) and insensitive (1021 cm^{-1}) peaks are visible. Each spectrum is the average of 5 spectra. (B) The calibration curve is plotted based on the 1034−1021 cm^{-1} intensity ratio measured at each Zn^{2+} concentration.

NCs@TPY at different pH values and up to 6 months of storage time.

Calibration Curve between Zn^{2+} Concentration in Biological Media and Ratiometric SERS Sensing. Next, we validated that our nanosensor can react with different amounts of Zn^{2+} in a biologically relevant environment. This is a highly complex media compared to others like saline buffers or water due to the presence of proteins, other biomolecules, and a high ionic strength, all affecting the Raman scattering signal-to-noise ratio.

First, we filtered out cations from the cellular medium and implemented it with different amounts of Zn^{2+}, and then, we added the NCs@TPY and recorded the SERS signal. It is worth noting that the spectrum of TPY changes when the NCs@TPY was dispersed in water (Figure S1C) as in the growth medium (Figure S3A). The intensity of the Raman signal at different shifts (1034, 1327, 1463, and 1530−1598 cm^{-1}) increases along with the Zn^{2+} concentration, whereas the Raman shift of the main ring-breathing mode at 1021 cm^{-1} of the TPY ligand[24,29] was Zn^{2+}- and dispersant-independent and remained unaltered (cf., Figure S3A). We calculated the ratio between all zinc-sensitive bands and the nonsensitive (1021 cm^{-1}) band. Ratiometric measurements allow the signal being independent from external factors like differences in batch-to-batch or in cell loading.[30] Except for the Raman shift at 1034 cm^{-1}, other ratios did not show a dependency on Zn^{2+} concentrations (Figure 3A; cf., Figure S3B,D).

The intensity of the Raman signal at 1034 cm^{-1} increases with the Zn^{2+} concentration. This peak is assigned to an ion-induced shift of the main ring-breathing mode (1021 cm^{-1}). Zn^{2+} sensing occurs then by the increase of a SERS peak at 1034 cm^{-1}, relative to the standard peak at 1021 cm^{-1}. Finally, we built a calibration curve between each Zn^{2+} concentration and the corresponding ratiometric signal (I_{1034}/I_{1021}) of NCs@TPY (Figure 3B). A regression analysis allows prediction of unknown Zn^{2+} amounts based on the SERS signal. There is good linearity (R^2 = 0.98) and high sensitivity [limit of detection (LOD) = $10^{-11.72}$ M] (Figure 3B).

A big concern in ion sensing is the selectivity of the sensor. For example, the cadmium signal cross-talks with the Zn^{2+} signal due to their similar electronic structure. How to avoid this interference is argued. Nevertheless, cadmium exists in biological/physiological samples at extremely low concentrations because of its toxic nature.[31] On the contrary, calcium is a signal biomolecule potentially interfering with pyridine sensors, and it is present in biological samples at high concentrations. Despite some reports neglecting the interference of calcium,[32] we decided to analyze the selectivity of NCs@TPY toward Zn^{2+} in the presence of calcium. As shown in Figure S4, the peaks associated with calcium sensing shift compared to those associated with Zn^{2+} sensing. For example, the cation-sensitive peak shifts from 1034 cm^{-1} for Zn^{2+} to 1037 cm^{-1} for calcium, and the cation-insensitive peak shifts from 1021 cm^{-1} in the presence of Zn^{2+} to 1026 cm^{-1} in the presence of calcium. The peak at 1037 cm^{-1}, although changing toward calcium, did not show a trend. We observed that the peak at 1002 cm^{-1} decreased with increasing calcium amounts.

Other research studies (Lee[33] and Li[34]) also used a Raman probe with similar pyridine groups to detect cations like Ca^{2+}, Mg^{2+}, Mn^{2+}, and Zn^{2+}. Their results showed that metal ions other than Zn^{2+} do not exhibit a significant response. Cd^{2+} has a similar electronic structure to Zn^{2+} and, therefore, serves as the main interference for Zn^{2+}. Nevertheless, although there is Cd^{2+} in the environment and biological samples, their concentrations are extremely low because of its high cytotoxicity. Just as we did for Ca^{2+} and Zn^{2+}, they also reported a shift in the SERS signal of the Raman probe when chelated to Zn^{2+} or to Cd^{2+}. This may occur because of the difference existing in the effective coordination of Zn^{2+} and Cd^{2+} to the pyridine group.[35] Compared with Zn^{2+}, Cd^{2+} has a larger ionic radius and is a weaker Lewis acid. According to Hancock's "steric crowding" effect,[36−38] increasing the number of chelate rings of a complex from five-membered to six-membered rings increases the stability of the smaller metal ionic complex relative to that of the larger metal ionic complex. And Zn^{2+} is more likely to form six-membered chelate rings with the terpyridine ligand, thus exhibiting a higher affinity.

Many reports involving coordination of metal ions and ligands are explained by the theory of hard-soft-acid-base

https://doi.org/10.1021/acsomega.4c03631
ACS Omega 2024, 9, 42183−42192

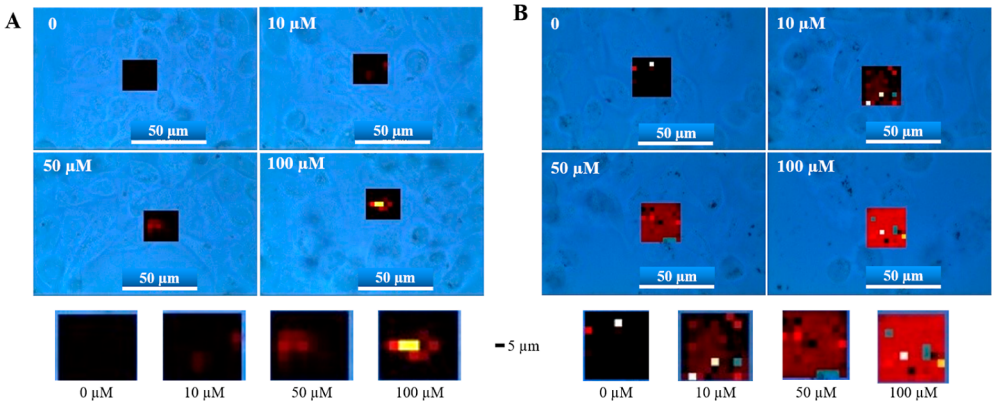

Figure 4. Intracellular Zn^{2+} SERS mapping. MDA (A) and MDA-Zip4 (B) were incubated with NCs@TPY for 24 h and were exposed to different amounts of Zn^{2+} (0, 10, 50, and 100 μM) for 2 h. The measured area is 23 (l) × 21 (w) μm, and during each mapping, we acquired 56 spectra/area. Increasing values of the sensitive vs insensitive band ratio (I_{1034}/I_{1021}) correspond to an increase in the colored (red) area. A zoomed-in view of the scanned area is shown (scale bar 5 μm).

(HSAB), which was first proposed in 1963 by Pearson.[39] The principle behind this theory is that "hard acids prefer to coordinate to hard bases and soft acids to soft bases". Lewis acids and bases can be classified by being designated as hard or soft. Some acids and bases with intermediate character, between hard and soft, are classified as borderline. Zn^{2+} is a borderline acid that prefers to bind a borderline base such as the pyridine group.[40] But Ca^{2+} is classified as hard acid, which prefers to bind to a hard base like carboxylate oxygen.[41] Altogether, it indicates that our Raman probe TPY has more affinity for Zn^{2+} than for Ca^{2+}.

Intracellular Zn^{2+} Sensing in Metastatic and Parental Breast Cancer Cells. Triple-negative breast cancer is a metastatic cancer that easily metastasizes. We selected four types of breast cancer cells potentially differing in their amounts of Zn^{2+} to validate our nanosensor. We took two metastatic cell lines, isolated from breast metastasis in the brain (BrM2) and lung (LM2), one parental (MDA, nonmetastatic), and this last one overexpressing the Zip4 receptor contributing to the cellular diffusion of Zn^{2+} (MDA-Zip4). In this way, we wanted to measure a possible relationship between the Zn^{2+} amount and pro-metastatic features.

First of all, we proved if external addition of Zn^{2+} to the cells had an effect on the intracellular amount of the ion (Figure 4; cf., Figure S5). We incubated MDA and MDA-Zip4 cells with different amounts of Zn^{2+} and measured the intracellular amount with the standard fluorescent Zn^{2+} sensor, Zinquin.[42−44] Figure S5A,B confirms the increase of intracellular Zn^{2+} depending on the amount externally added. Furthermore, we incubated both cell types with our nanosensor and monitored the intracellular Zn^{2+} increase by mapping the living cells exposed to different Zn^{2+} amounts (Figure 4). Interestingly, we observed that the cells overexpressing the Zn^{2+} receptor, Zip4, internalized more Zn^{2+} than their counterparts (Figure 4), contrarily to the standard fluorescent Zn^{2+} probe that measured no difference between the cells (cf., Figure S5).

After confirming the responsiveness of our nanosensor to Zn^{2+} dynamics, we measured the intracellular (cf., Figure S6) and extracellular (cf., Figure S7) Zn^{2+} amounts of the metastatic and parental cells. We wanted to see the effect of external addition of Zn^{2+} to the intracellular and extracellular Zn^{2+} amounts. We exposed the cells to different amounts of Zn^{2+} in a cation-depleted GM. We measured the SERS intensity of internalized and extracellular individual nanosensors, and we calculated the ratio of the sensitive vs nonsensitive band (I_{1034}/I_{1021}) and made the average of all measurements (Figure 5; cf., Figures S6 and S7). Figure 5 shows the ratiometric intracellular SERS signal, and Table 1 shows the quantitative values of the intracellular amount for all cell types (cf., Table S1 for the extracellular Zn^{2+} amount).

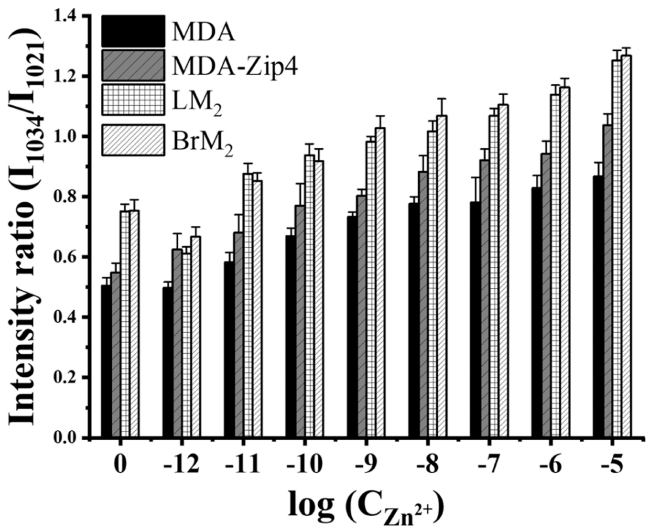

Figure 5. Zn^{2+}quantification in metastatic and parental breast tumor cells. (A) Different breast cancer cells (MDA, MDA-Zip4, LM2, and BrM2 cells) were cultured in growth medium supplemented with different amounts of Zn^{2+} (10^{-5}, 10^{-6}, 10^{-7}, 10^{-8}, 10^{-9}, 10^{-10}, 10^{-11}, and 10^{-12} M and none). NCs@TPY quantified the intracellular Zn^{2+} amount based on the intensity ratio of the sensitive (1034 cm^{-1}) to insensitive (1021 cm^{-1}) band.

Compared to their intracellular basal levels, all cells increased their intracellular Zn^{2+} amount after external Zn^{2+} addition (10^{-5} to 10^{-11} M) except for that at 10^{-12} M, which is reduced. Since our LOD is $10^{-11.72}$ M, the quantification in this range may not be accurate. The extracellular Zn^{2+} quantification exhibited increasing levels of labile zinc (compared to extracellular basal levels) with the addition of Zn^{2+}, although these values are below our LOD. Considering the amount added, we do not exclude that labile zinc homeostasis is altered by the presence of serum proteins and this is why we measure

https://doi.org/10.1021/acsomega.4c03631
ACS Omega 2024, 9, 42183−42192

Table 1. Quantitative Values of the Intracellular Zn^{2+} Amount for All Cell Types and the LOD of Our Zn^{2+} Nanosensor[a]

Zn^{2+} (M) added	MDA	MDA-Zip4	LM2	BrM2
0	$10^{-14.42}$	$10^{-13.74}$	$10^{-10.52}$	$10^{-10.48}$
10^{-5}	$10^{-8.67}$	$10^{-5.98}$	$10^{-2.56}$	$10^{-2.31}$
10^{-6}	$10^{-9.28}$	$10^{-7.49}$	$10^{-4.36}$	$10^{-3.99}$
10^{-7}	$10^{-10.04}$	$10^{-7.81}$	$10^{-5.47}$	$10^{-4.90}$
10^{-8}	$10^{-10.11}$	$10^{-8.43}$	$10^{-6.30}$	$10^{-5.47}$
10^{-9}	$10^{-10.80}$	$10^{-9.70}$	$10^{-6.85}$	$10^{-6.13}$
10^{-10}	$10^{-11.81}$	$10^{-10.21}$	$10^{-7.56}$	$10^{-7.97}$
10^{-11}	$10^{-13.20}$	$10^{-11.63}$	$10^{-8.53}$	$10^{-8.91}$
10^{-12}	$10^{-14.54}$	$10^{-12.52}$	$10^{-12.74}$	$10^{-11.86}$
LOD	$10^{-11.72}$			

[a](cf., Table S1 for the extracellular values).

such low extracellular levels. The MDA-Zip4 cells overexpressing Zip4 have higher intracellular labile zinc amounts than the control MDA cells. Also, their basal levels are increased. To the best of our knowledge, it has not been published whether the overexpression of Zip4 influences the other members of the Zip family. We know that MDA-Zip4 cells express 3 times Zip4 than MDA;[42,45] therefore, all this could point to a significant role of Zip4 in regulating the entry of external Zn^{2+}.

In general, we can conclude that metastatic cells (LM2 and BrM2) exhibited similar amounts of labile zinc content, and both showed much higher intracellular and extracellular values than the parental cells (MDA and MDA-Zip4).

When analyzing these results in more detail (Figure 6), we observed several effects. The basal levels of labile zinc (without external addition) in the metastatic cells (LM2 and BrM2) are significantly higher than those in the parental cells (MDA and MDA-Zip4) (Figure 6A; cf., Figures S8 and S9). As the concentration of Zn^{2+} in the cation-depleted culture medium increased, the ability of LM2 and BrM2 cells to take up Zn^{2+} was significantly enhanced compared to that of MDA cells. In addition, when analyzing the Zn^{2+} increment with respect to its basal level after the external addition of Zn^{2+} (Figure 6B; cf., Figures S8 and S9), there is an increase of the slope of the straight line following the trend BrM2 > LM2 ≫ MDA-Zip4 > MDA. Figure 6C shows the level of increase of the amount of Zn^{2+} per type of cell compared to their basal level.

These results conclude that the amount of Zn^{2+} in brain and lung metastatic cells is significantly higher than in the parental cells, a result consistent with published results.[42] Since we could quantify more labile zinc in metastatic cells than the parental one, we notice a correlation between Zn^{2+} homeostasis and metastasis of breast cancer cells.

CONCLUSIONS

We successfully synthesized an ultrasensitive nanosensor (NCs@TPY) for free Zn^{2+} detection, which is composed of a complex of NCs and the TPY Raman probe. NCs are formed by ensembles of gold nanoparticles and a silica shell, which can

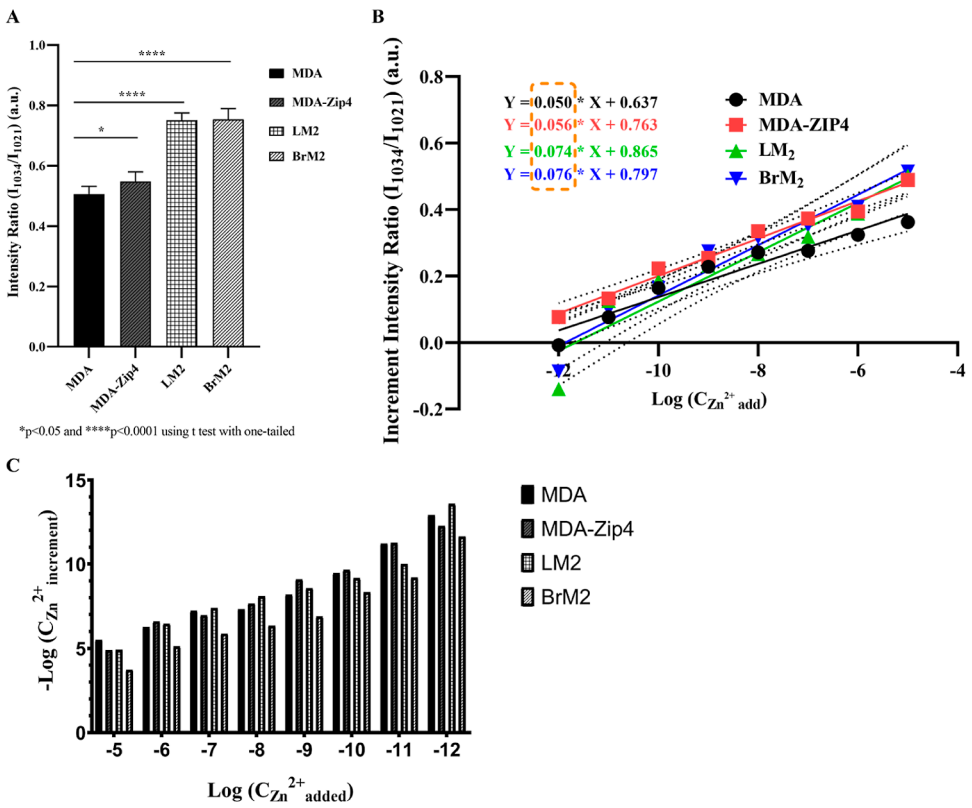

Figure 6. Differences of basal intracellular Zn^{2+} and Zn^{2+} acquisition capacity in different cells. (A) Different breast cancer cells (MDA, MDA-Zip4, LM2, and BrM2 cells) were cultured with NCs@TPY and exposed to ion-depleted GM without Zn^{2+} addition overnight. (B) Cells were also exposed to ion-depleted GM supplemented with different amounts of Zn^{2+} (10^{-5}, 10^{-6}, 10^{-7}, 10^{-8}, 10^{-9}, 10^{-10}, 10^{-11}, and 10^{-12} M) overnight, and then, the basal level of Zn^{2+} was removed in each cell line. NCs@TPY quantified their intracellular Zn^{2+} amount based on the intensity ratio of the sensitive (1034 cm^{-1}) to insensitive (1021 cm^{-1}) band. (C) Quantitative values of the increment of Zn^{2+} from each cell line.

https://doi.org/10.1021/acsomega.4c03631
ACS Omega 2024, 9, 42183−42192

not only generate "hot spots" at the internal interface but also prevent physicochemical interaction between the gold nanoparticles and the big biomolecules from biological media. Moreover, the TPY molecule, with narrow a Raman cross-section, rapidly chelates Zn^{2+} tightly and has a high affinity to Zn^{2+} compared to that to the other cations. The sensor quantifies Zn^{2+} in the range of 10^{-5} to 10^{-11} M, with a low LOD at $10^{-11.72}$ M and good linearity $R^2 = 0.98$. Although NCs were colocalized within lysosomes with luminal acidic pH, the Raman signal of our nanosensor is stable from pH 3 to pH 9. The nanosensor was tested in metastatic and parental breast cancer cell lines to quantify possible differences in Zn^{2+} content related to the nature of the cell. We found out that the metastatic cell has more intracellular Zn^{2+} than the parental one and has the ability to take up more Zn^{2+}. Here, we report a reliable nanosensor for quantifying Zn^{2+} within cells.

■ ASSOCIATED CONTENT

Supporting Information

The Supporting Information is available free of charge at https://pubs.acs.org/doi/10.1021/acsomega.4c03631.

Additional results and methodology and additional information on all the sections of the article from the synthesis to the biological zinc quantification (PDF)

■ AUTHOR INFORMATION

Corresponding Author

Pilar Rivera-Gil − *Integrative Biomedical Materials and Nanomedicine Laboratory, Department of Medicine and Life Sciences, Universitat Pompeu Fabra, PRBB, Barcelona 08003, Spain;* orcid.org/0000-0002-6587-7538; Email: pilar.rivera@upf.edu

Authors

Ting Zhou − *Integrative Biomedical Materials and Nanomedicine Laboratory, Department of Medicine and Life Sciences, Universitat Pompeu Fabra, PRBB, Barcelona 08003, Spain;* orcid.org/0000-0003-4098-4801

Rubén Vicente − *Molecular Physiology Laboratory, Department of Medicine and Life Sciences, Universitat Pompeu Fabra, PRBB, Barcelona 08003, Spain*

Complete contact information is available at: https://pubs.acs.org/10.1021/acsomega.4c03631

Notes

The authors declare no competing financial interest.

■ ACKNOWLEDGMENTS

Pilar Rivera Gil acknowledges the Ministry of Science, Innovation and Universities (MICINN) and the AEI (AEI-PID2019-106755RB-I00 and PID2022-140423NB-I00) and the AGAUR (2021 SGR 00175 and 2021 PROD 00041) for financial support. T.Z. and Pilar Rivera Gil appreciate the financial support from the China Scholarship Council (CSC) by a State Scholarship Fund (NSCIS no. 202008350121). R.V. acknowledges AEI (PID2022-136511OB-I00) for financial support.

■ REFERENCES

(1) Zhang, X.-a.; Lovejoy, K. S.; Jasanoff, A.; Lippard, S. J. Water-soluble porphyrins as a dual-function molecular imaging platform for MRI and fluorescence zinc sensing. *Proc. Natl. Acad. Sci. U.S.A.* **2007**, *104* (26), 10780−10785.

(2) Hambidge, M. Human zinc deficiency. *J. Nutr.* **2000**, *130* (5), 1344S−1349S.

(3) Craddock, T. J.; Tuszynski, J. A.; Chopra, D.; Casey, N.; Goldstein, L. E.; Hameroff, S. R.; Tanzi, R. E. The zinc dyshomeostasis hypothesis of Alzheimer's disease. *PLoS One* **2012**, *7* (3), No. e33552.

(4) Yan, X.; Kim, J. J.; Jeong, H. S.; Moon, Y. K.; Cho, Y. K.; Ahn, S.; Jun, S. B.; Kim, H.; You, Y. Low-Affinity Zinc Sensor Showing Fluorescence Responses with Minimal Artifacts. *Inorg. Chem.* **2017**, *56* (8), 4332−4346.

(5) Frederickson, C. J.; Suh, S. W.; Silva, D.; Frederickson, C. J.; Thompson, R. B. Importance of zinc in the central nervous system: the zinc-containing neuron. *J. Nutr.* **2000**, *130* (5), 1471S−1483S.

(6) Kim, J. W.; Byun, M. S.; Yi, D.; Lee, J. H.; Kim, M. J.; Jung, G.; Lee, J. Y.; Kang, K. M.; Sohn, C. H.; Lee, Y. S.; et al. Serum zinc levels and in vivo beta-amyloid deposition in the human brain. *Alzheimers Res. Ther* **2021**, *13* (1), 190.

(7) Fukunaka, A.; Fujitani, Y. Role of Zinc Homeostasis in the Pathogenesis of Diabetes and Obesity. *Int. J. Mol. Sci.* **2018**, *19* (2), 476.

(8) Dhawan, D. K.; Chadha, V. D. Zinc: A promising agent in dietary chemoprevention of cancer. *Indian J. Med. Res.* **2010**, *132* (6), 676−682.

(9) Wenzlau, J. M.; Juhl, K.; Yu, L.; Moua, O.; Sarkar, S. A.; Gottlieb, P.; Rewers, M.; Eisenbarth, G. S.; Jensen, J.; Davidson, H. W.; et al. The cation efflux transporter ZnT8 (Slc30A8) is a major autoantigen in human type 1 diabetes. *Proc. Natl. Acad. Sci. U.S.A.* **2007**, *104* (43), 17040−17045.

(10) Goldberg, J. M.; Lippard, S. J. Mobile zinc as a modulator of sensory perception. *FEBS Lett.* **2023**, *597* (1), 151−165.

(11) Zhou, T.; Lu, D.; She, Q.; Chen, C.; Chen, J.; Huang, Z.; Feng, S.; You, R.; Lu, Y. Hypersensitive detection of IL-6 on SERS substrate calibrated by dual model. *Sens. Actuators, B* **2021**, *336*, 129597.

(12) Zhou, T.; Fan, M.; You, R.; Lu, Y.; Huang, L.; Xu, Y.; Feng, S.; Wu, Y.; Shen, H.; Zhu, L. Fabrication of Fe(3)O(4)/Au@ATP@Ag Nanorod sandwich structure for sensitive SERS quantitative detection of histamine. *Anal. Chim. Acta* **2020**, *1104*, 199−206.

(13) Xiao, C.; Izquierdo-Roca, V.; Rivera-Gil, P. Real Time and Spatiotemporal Quantification of pH and H(2)O(2) Imbalances with a Multiplex Surface-Enhanced Raman Spectroscopy Nanosensor. *ACS Mater. Au* **2023**, *3* (2), 164−175.

(14) Lu, Y.; Zhou, T.; You, R.; Wu, Y.; Shen, H.; Feng, S.; Su, J. Fabrication and Characterization of a Highly-Sensitive Surface-Enhanced Raman Scattering Nanosensor for Detecting Glucose in Urine. *Nanomaterials (Basel)* **2018**, *8* (8), 629.

(15) Rivera_Gil, P.; Vazquez-Vazquez, C.; Giannini, V.; Callao, M. P.; Parak, W. J.; Correa-Duarte, M. A.; Alvarez-Puebla, R. A. Plasmonic nanoprobes for real-time optical monitoring of nitric oxide inside living cells. *Angew. Chem., Int. Ed. Engl.* **2013**, *52* (51), 13694−13698.

(16) García-Algar, M.; Tsoutsi, D.; Sanles-Sobrido, M.; Cabot, A.; Izquierdo-Roca, V.; Gil, H. P. R. Subcellular Optical pH Nanoscale Sensor. *ChemistrySelect* **2017**, *2* (26), 8115−8121.

(17) Sanles-Sobrido, M.; Exner, W.; Rodríguez-Lorenzo, L.; Rodríguez-González, B.; Liz-Marzán, L. M.; Correa-Duarte, M. A.; Álvarez-Puebla, R. A. Design of SERS-Encoded, Submicron, Hollow Particles Through Confined Growth of Encapsulated Metal Nanoparticles. *J. Am. Chem. Soc.* **2009**, *131* (7), 2699−2705.

(18) Šloufová, I.; Vlčková, B.; Mojzeš, P.; Matulková, I.; Císařová, I.; Procházka, M.; Vohlídal, J. Probing the Formation, Structure, and Reactivity of Zn(II), Ag(I), and Fe(II) Complexes with 2,2′:6′,2″-Terpyridine on Ag Nanoparticles Surfaces by Time Evolution of SERS Spectra, Factor Analysis, and DFT Calculations. *J. Phys. Chem. C* **2018**, *122* (11), 6066−6077.

(19) Constable, E. C.; Hermann, B. A.; Housecroft, C. E.; Neuburger, M.; Schaffner, S.; Scherer, L. J. 2,2′:6′,2″-Terpyridine-

4′(1′H)-thione: a missing link in metallosupramolecular chemistry. *New J. Chem.* **2005**, *29* (11), 1475.
(20) Eilers, P.; Boelens, H. Baseline Correction with Asymmetric Least Squares Smoothing. *Life Sci.* **2005**, *1*, 1−26.
(21) Tsoutsi, D.; Sanles-Sobrido, M.; Cabot, A.; Gil, P. R. Common Aspects Influencing the Translocation of SERS to Biomedicine. *Curr. Med. Chem.* **2018**, *25* (35), 4638−4652.
(22) Nyamekye, C. K. A.; Weibel, S. C.; Smith, E. A. Directional Raman scattering spectra of metal-sulfur bonds at smooth gold and silver substrates. *J. Raman Spectrosc.* **2021**, *52* (7), 1246−1255.
(23) Osterloh, F.; Hiramatsu, H.; Porter, R.; Guo, T. Alkanethiol-Induced Structural Rearrangements in Silica−Gold Core−Shell-type Nanoparticle Clusters: An Opportunity for Chemical Sensor Engineering. *Langmuir* **2004**, *20*, 5553−5558.
(24) Zhao, Y.; Newton, J. N.; Liu, J.; Wei, A. Dithiocarbamate-coated SERS substrates: sensitivity gain by partial surface passivation. *Langmuir* **2009**, *25* (24), 13833−13839.
(25) Wright, D.; Lin, Q.; Berta, D.; Földes, T.; Wagner, A.; Griffiths, J.; Readman, C.; Rosta, E.; Reisner, E.; Baumberg, J. J. Mechanistic study of an immobilized molecular electrocatalyst by in situ gap-plasmon-assisted spectro-electrochemistry. *Nature Catalysis* **2021**, *4* (2), 157−163.
(26) Hühn, D.; Kantner, K.; Geidel, C.; Brandholt, S.; De Cock, I.; Soenen, S. J. H.; Rivera_Gil, P.; Montenegro, J. M.; Braeckmans, K.; Müllen, K.; Nienhaus, G. U.; Klapper, M.; et al. Polymer-Coated NanoparticlesInteracting with Proteins and Cells:Focusing on the Sign of the Net Charge. *ACS Nano* **2013**, *7* (4), 3253−3263.
(27) Jiang, X.; Valdeperez, D.; Nazarenus, M.; Wang, Z.; Stellacci, F.; Parak, W. J.; del Pino, P. Future Perspectives Towards the Use of Nanomaterials for Smart Food Packaging and Quality Control. *Particle & Particle Systems Characterization* **2015**, *32* (4), 408−416.
(28) Abhijnakrishna, R.; Magesh, K.; Ayushi, A.; Velmathi, S. Advances in the Biological Studies of Metal-Terpyridine Complexes: An Overview From 2012 to 2022. *Coord. Chem. Rev.* **2023**, *496*, 215380.
(29) Sant'Ana, A. C.; Alves, W. A.; Santos, R. H. A.; Ferreira, A. M. D.; Temperini, M. L. A. The adsorption of 2,2′:6′,2″-terpyridine, 4′-(5-mercaptopentyl)-2,2′:6′,2″-terpyridinyl, and perchlorate on silver and copper surfaces monitored by SERS. *Polyhedron* **2003**, *22* (13), 1673−1682.
(30) Carregal-Romero, S.; Montenegro, J. M.; Parak, W. J.; Rivera_Gil, P. Subcellular carrier-based optical ion-selective nano-sensors. *Front. Pharmacol* **2012**, *3*, 70.
(31) Peana, M.; Pelucelli, A.; Chasapis, C. T.; Perlepes, S. P.; Bekiari, V.; Medici, S.; Zoroddu, M. A. Biological Effects of Human Exposure to Environmental Cadmium. *Biomolecules* **2022**, *13* (1), 36.
(32) Jin, L.; She, G.; Mu, L.; Shi, W. Highly uniform indicator-mediated SERS sensor platform for the detection of Zn2+. *RSC Adv.* **2016**, *6* (20), 16555−16560.
(33) Lee, N.; Ly, N. H.; Kim, J. S.; Jung, H. S.; Joo, S.-W. A selective triarylmethine-based spectroscopic probe for Zn2+ ion monitoring. *Dyes Pigm.* **2019**, *171*, 107721.
(34) Li, D.; Ma, Y.; Duan, H.; Jiang, F.; Deng, W.; Ren, X. Fluorescent/SERS dual-sensing and imaging of intracellular Zn2+. *Anal. Chim. Acta* **2018**, *1038*, 148−156.
(35) Zhu, L.; Yuan, Z.; Simmons, J. T.; Sreenath, K. Zn(II)-coordination modulated ligand photophysical processes - the development of fluorescent indicators for imaging biological Zn(II) ions. *RSC Adv.* **2014**, *4* (39), 20398−20440.
(36) Hancock, R. D.; Martell, A. E. Ligand design for selective complexation of metal ions in aqueous solution. *Chem. Rev.* **1989**, *89* (8), 1875−1914.
(37) Hancock, R. D. Molecular mechanics calculations and metal ion recognition. *Acc. Chem. Res.* **1990**, *23* (8), 253−257.
(38) Ejarque, D.; Calvet, T.; Font-Bardia, M.; Pons, J. Steric crowding of a series of pyridine based ligands influencing the photophysical properties of Zn(II) complexes. *CrystEngComm* **2021**, *23* (35), 6199−6213.
(39) Pearson, R. G. Hard and Soft Acids and Bases. *J. Chem. Educ.* **1968**, *45* (9), 581.
(40) Pearson, R. G. Hard and soft acids and bases, HSAB, part 1: Fundamental principles. *J. Chem. Educ.* **1968**, *45* (9), 581.
(41) Wang, S.; Cao, J.; Jia, W.; Guo, W.; Yan, S.; Wang, Y.; Zhang, P.; Chen, H. Y.; Huang, S. Single molecule observation of hard-soft-acid-base (HSAB) interaction in engineered Mycobacterium smegmatis porin A (MspA) nanopores. *Chem. Sci.* **2020**, *11* (3), 879−887.
(42) Vogel-Gonzalez, M.; Musa-Afaneh, D.; Rivera Gil, P.; Vicente, R. Zinc Favors Triple-Negative Breast Cancer's Microenvironment Modulation and Cell Plasticity. *Int. J. Mol. Sci.* **2021**, *22* (17), 9188.
(43) Nowakowski, A. B.; Petering, D. H. Reactions of the fluorescent sensor, Zinquin, with the zinc-proteome: adduct formation and ligand substitution. *Inorg. Chem.* **2011**, *50* (20), 10124−10133.
(44) Zalewski, P. D.; Forbes, I. J.; Betts, W. H. Correlation of apoptosis with change in intracellular labile Zn(II) using Zinquin [(2-methyl-8-p-toluenesulphonamido-6-quinolyloxy)acetic acid], a new specific fluorescent probe for Zn(II). *Biochem. J.* **1993**, *296*, 403−408.
(45) Chen, Q. G.; Zhang, Z.; Yang, Q.; Shan, G. Y.; Yu, X. Y.; Kong, C. Z. The role of zinc transporter ZIP4 in prostate carcinoma. *Urol Oncol* **2012**, *30* (6), 906−911.

https://doi.org/10.1021/acsomega.4c03631
ACS Omega 2024, 9, 42183−42192